Nano Research
2020, 13(12): 3321–3329
ISSN 1998-0124 CN 11-5974/O4
https://doi.org/10.1007/s12274-020-3010-7

Research Article

Noble-metal-free catalyst with enhanced hydrogen evolution reaction activity based on granulated Co-doped Ni-Mo phosphide nanorod arrays

Heping Xie[1,2] (✉), Cheng Lan[1,2], Bin Chen[2], Fuhuan Wang[2,3], and Tao Liu[1]

[1] *Institute of New Energy and Low-Carbon Technology, Sichuan University, Chengdu 610065, China*
[2] *Guangdong Provincial Key Laboratory of Deep Earth Sciences and Geothermal Energy Exploitation and Utilization, Institute of Deep Earth Sciences and Green Energy, Shenzhen University, Shenzhen 518060, China*
[3] *School of Chemical Engineering, Sichuan University, Chengdu 610065, China*

Received: 16 May 2020 / **Revised:** 8 July 2020 / **Accepted:** 26 July 2020

ABSTRACT

The development of noble-metal-free electrocatalysts for water splitting is indispensable for the efficient production of hydrogen fuel. Herein, a Co-doped Ni-Mo phosphide nanorod arrays fabricated on porous Ni foam was shown to be an efficient binder-free electrocatalyst for water splitting. This catalyst featured exceptional activity, exhibiting an overpotential of 29 mV at a current density of 10 mA·cm^{-2} for the hydrogen evolution reaction, whereas the corresponding precatalyst exhibited an overpotential of 314 mV at a current density of 50 mA·cm^{-2} for the oxygen evolution reaction. The achieved electrocatalytic performance provided access to a simple water splitting system, affording a current density of 10 mA·cm^{-2} at 1.47 V in 1 M KOH electrolyte. Density functional theory results indicated that Co doping and phosphorization were responsible for the high electrocatalytic performance. Thus, this work paves the way for the development of novel noble-metal-free electrocatalysts for practical H_2 production via water splitting.

KEYWORDS

noble-metal-free electrocatalyst, overall water splitting, cobalt doping, phosphorization, granulated morphology

1 Introduction

Water splitting is a promising method for the highly efficient conversion and storage of energy from intermittent sources (e.g., wind and solar energy). As this process affords renewable hydrogen, it's therefore considered an excellent solution to the global energy and environmental crisis [1, 2]. Electrocatalysts with enhanced activity and stability are necessary to trigger overall water electrolysis, comprising the cathodic hydrogen evolution reaction (HER) and the anodic oxygen evolution reaction (OER) [3, 4]. Pt/C and RuO_2 (or IrO_2) have been widely considered benchmark catalysts owing to their ability to lower the HER and OER activation barriers, respectively, and thus enhance the corresponding kinetics. However, since the scarcity and high cost of these noble metals hinder their large-scale commercial applications in overall water splitting [5–7]. As a result, considerable effort has been directed toward the development of nonprecious transition-metal-based catalysts for the OER and HER [8, 9]. Therefore, the design and synthesis of noble-metal-free electrocatalysts for overall water splitting are of high practical significance [10–13].

Transition metal doping, especially Co doping, has attracted much interest as a technique to improve the electron conductivity and activity of electrocatalysts [14–18]. For instance, Xu et al. used Co doping to improve the intrinsic electrocatalytic HER activity of $NiPS_3$, achieving a geometric catalytic current density of 10 mA·cm^{-2} at an overpotential of 71 mV vs. reversible hydrogen electrode (RHE) in 1 M KOH electrolyte [19]. Liu et al. reported a hierarchical $CoMoS_x$ chalcogel on a Ni foam synthesized through an *in-situ* metathesis reaction. This electrocatalyst realized a current density of 100 mA·cm^{-2} below 1.74 V, which is lower than that of MoS_x without Co doping (1.87 V) [20]. Dong et al. prepared Co-doped β-molybdenum carbide (β-Mo_2C) encapsulated by a N-doped carbon framework, which afforded a current density of 10 mA·cm^{-2} for the OER at a low overpotential of 1.6 V and provided a significant improvement in performance over β-Mo_2C (over 1.8 V) [21].

Therefore, an enhanced understanding of the factors that influence the catalytic activity of Co-doped catalysts should facilitate the development of advanced noble-metal-free electrocatalysts for water splitting.

Phosphorization enhances the performance of HER electrocatalysts, typically by producing changes in the ion valence state and nanomaterial morphology, with the emergence of hierarchical structures increasing the electrochemical surface area [22–27]. Moreover, P can form moderate bonds with the reaction intermediates, thus increasing the number of proton and hydride acceptor sites on the material surface [28]. As a representative example of the advances in using monometallic phosphides as electrocatalysts for water splitting, Ni-foil-supported Ni_5P_4 with a 3D hierarchical structure has exhibited an optimized catalytic activity with a low potential of 1.7 V at

Address correspondence to xiehp@szu.edu.cn

10 mA·cm^{-2} for overall water splitting [29]. Further, Co_2P/Co foil, synthesized by the one-step phosphorization of pre-oxidized Co foil, has exhibited overpotentials of 319 and 157 mV for the OER and HER (10 mA·cm^{-2}), respectively [30].

To achieve further improvements in catalytic activity, polymetallic phosphides have been widely explored because of their compositional diversity and potential synergism. For example, optimized-composition Co–Ni–P phosphides require a potential of only 1.511 V at a current density of 10 mA·cm^{-2} to catalyzed OER in alkaline solution, outperforming pure CoP and Ni_5P_4/Ni_2P [31]. Moreover, Ni_2P–CoP phosphides with strong interfacial effects were reported to exhibit significantly lower overpotentials than a simple mechanical mixture of Ni_2P and CoP electrocatalysts [32]. Therefore, the combination of transition metal doping and phosphorization holds great promise for the development of noble-metal-free water-splitting electrocatalysts.

Typically, Ni and Mo atoms provide a synergistic enhancement of the catalytic performance for the HER under alkaline conditions because of the balance between the adsorption strengths of Ni and Mo atoms with hydrogen atoms [33, 34]. Therefore, we have designed granulated Co-doped Ni–Mo phosphide nanorod arrays on Ni foam ($(NiMo)_{1-x}Co_xP$/NF) as a robust and efficient noble-metal-free electrocatalyst for overall water splitting in alkaline media. The reason of enhanced catalytic activity has been revealed to be the strong effects of Co doping and phosphorization on the nanorod arrays. Remarkably, phosphorization affects the ion valence state and catalyst morphology, enhancing the electrochemical activity. Therefore, the obtained electrode displays excellent catalytic activity for the HER (overpotential of 29 mV at 10 mA·cm^{-2}) and as the precatalyst also exhibits good OER catalytic activity (overpotential of 314 mV at 50 mA·cm^{-2}) in alkaline electrolytes, achieving an overall water splitting current density of 10 mA·cm^{-2} at a cell voltage of 1.47 V. Moreover, this water-splitting system has shown superior durability, as determined by an 88-h stability test.

2 Results and discussion

2.1 Catalyst characterization

The synthesis of $(NiMo)_{1-x}Co_xP$/NF is schematically outlined in Fig. 1, and similar procedures were used for the synthesis of $NiMoO_4$/NF, NiMoP/NF, $(NiMo)_{1-x}Co_xO_4$/NF, CoC/NF, and CoP/NF as comparative catalysts. Annealed Ni foam (Fig. S1 in the Electronic Supplementary Material (ESM)) was used as a substrate owing to its three-dimensional (3D) interconnected porous structure and excellent electrical conductivity. In the first step, $NiMoO_4$ nanorods were grown on Ni foam ($NiMoO_4$/NF) using a conventional hydrothermal method [33]. Scanning electron microscopy (SEM) imaging of this composite (Figs. S2(a) and S2(b) in the ESM) revealed that the Ni foam surface was evenly covered with dense nanorods (~ 100 nm in diameter). In the next step, a solution-phase method [20] was employed to produce the Co-doped $NiMoO_4$ precursor ($(NiMo)_{1-x}Co_xO_4$/NF) with an estimated Co content of ~ 1 wt.%, as determined by semi-qualitative elemental mapping (Fig. S3 in the ESM). Moreover, energy-dispersive X-ray spectroscopy (EDX) imaging of $(NiMo)_{1-x}Co_xO_4$/NF (Fig. S4(d) in the ESM) showed that Co was uniformly distributed in the nanorods. Finally, phosphorization with red phosphorus at 500 °C afforded $(NiMo)_{1-x}Co_xP$/NF as the desired product.

As illustrated in Figs. 2(a) and 2(b), $(NiMo)_{1-x}Co_xP$/NF featured $(NiMo)_{1-x}Co_xP$ nanorods with rugged and granulated morphologies. The nanorods were uniformly grown on the Ni foam surface and appeared to be wrapped in small piles with lengths of several micrometers and diameters of ~ 100 nm. Phosphorization-induced granulation was expected to enhance the electrocatalytic activity by increasing the electrochemical surface area and the number of active sites. Notably, abundant interconnections were observed in the 3D hierarchical structure of the nanorods grown on NF, which could facilitate electron transfer. Moreover, the void spaces between nanorods are expected to be beneficial for mass diffusion, i.e., the detachment of gas bubbles during the HER/OER [33].

X-ray powder diffraction (XRD) was employed to characterize nanorod phase composition. The XRD pattern of $(NiMo)_{1-x}Co_xP$/NF comprised peaks corresponding to the Ni foam substrate (JCPDS No. 04-0850), Ni_2P (JCPDS No. 74-1385), and $NiMoO_4$ (JCPDS No. 33-0948) (Fig. 2(c)). The presence of $NiMoO_4$ was mainly attributed to incomplete phosphorization. And another cause could be the unavoidable oxidation of the samples upon exposure to air [14, 33]. The XRD of patterns of $NiMoO_4$/NF, NiMoP/NF, and $(NiMo)_{1-x}Co_xO_4$/NF were shown in Fig. S4(f) in the ESM for comparison. A high-resolution transmission electron microscopy (HR-TEM) image and corresponding selected-area electron diffraction (SAED) pattern, employed to probe sample morphology and lattice structure, revealed the well-resolved lattice fringes (i.e., good crystallinity) of $(NiMo)_{1-x}Co_xP$ nanorods (Fig. 2(d)). The interplanar distance of 0.221 nm corresponded to the (111) plane of Ni_2P, whereas the interplanar distance of 0.351 nm was attributed to the $(\bar{1}12)$ plane of $NiMoO_4$. A high-angle annular dark-field scanning transmission electron microscopy (HAADF-STEM) image (Fig. 2(e)) and the corresponding elemental mapping of a single rod (Figs. 2(f)–2(i)) verified the successful synthesis of $(NiMo)_{1-x}Co_xP$ nanorods and the uniform distribution of Ni, Mo, Co, and P therein.

The surface elemental compositions and valence states of the nanorods on the Ni foam electrode were probed by X-ray photoelectron spectroscopy (XPS). Figure S5(a) in the ESM shows that the synthesized sample $(NiMo)_{1-x}Co_xP$/NF contains Ni, Mo, Co, P, C, and O. The expected elements were also observed for the precursor $NiMoO_4$/NF (Fig. S6(a) in the ESM) and the intermediate product $(NiMo)_{1-x}Co_xO_4$/NF (Fig. S7(a) in the ESM). The presence of C was ascribed to residual adhesive carbon tape used for sample fixation during measurements

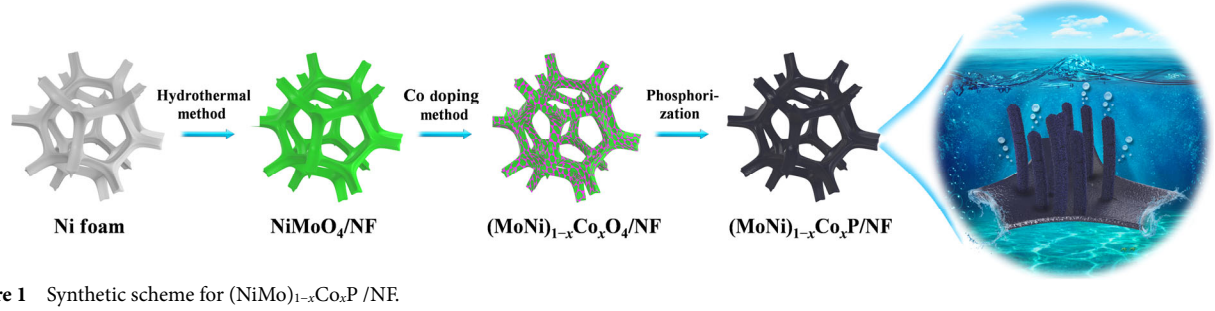

Figure 1 Synthetic scheme for $(NiMo)_{1-x}Co_xP$ /NF.

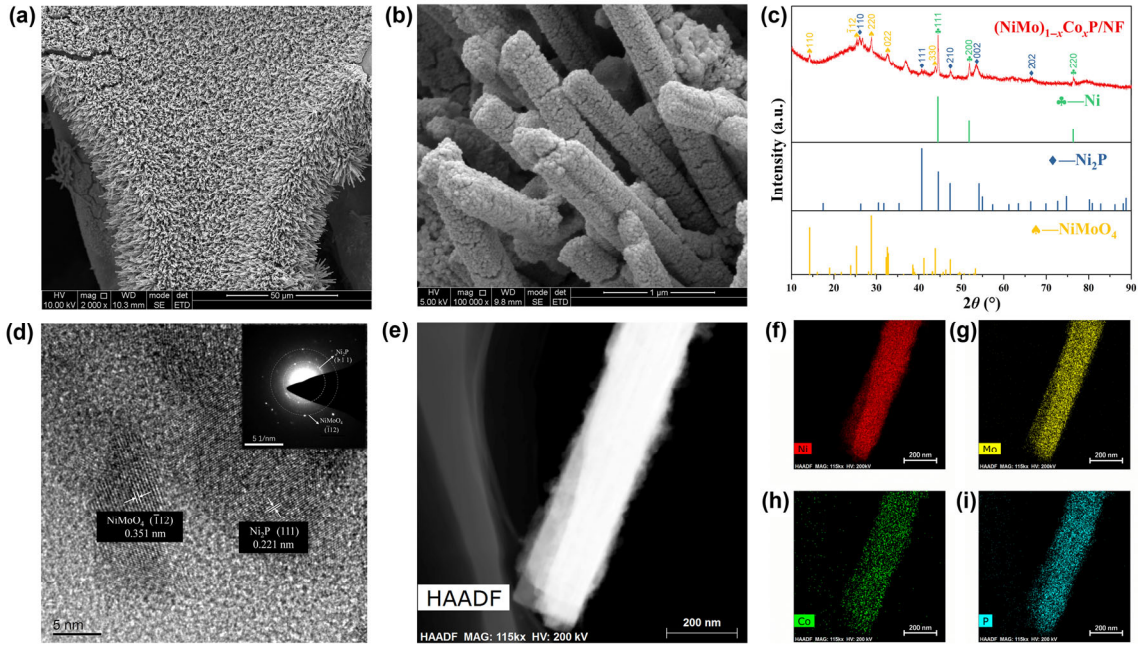

Figure 2 (a) Low-magnification and (b) high-magnification SEM images of $(NiMo)_{1-x}Co_xP$ nanorod arrays on Ni foam. (c) XRD patterns of $(NiMo)_{1-x}Co_xP$/NF, Ni, Ni_2P, and $NiMoO_4$. (d) HR-TEM image and corresponding SAED pattern of a $(NiMo)_{1-x}Co_xP$ nanorod. (e) HAADF-STEM image of a $(NiMo)_{1-x}Co_xP$ nanorod. (f)–(i) EDX elemental mappings of Ni, Mo, Co, and P, respectively.

[33, 35]. The Ni 2p peaks of $(NiMo)_{1-x}Co_xP$/NF (Fig. S5(b) in the ESM) at 855.7 and 873.4 eV were assigned to Ni $2p_{3/2}$ and Ni $2p_{1/2}$ orbitals, indicating the presence of Ni^{2+} at the surface. In addition, two broad satellite peaks were detected at 861.3 and 879.8 eV [33, 36]. The Mo 3d spectrum of $(NiMo)_{1-x}Co_xO_4$/NF (Fig. 3(a)) featured peaks attributed to Mo^{6+} centered at 232.1 and 235.2 eV [37]. After phosphorization, peaks attributable to new Mo species appeared in the Mo 3d spectrum of $(NiMo)_{1-x}Co_xP$/NF (Fig. 3(b)). The peaks at 229.4 and 230.53 eV were ascribed to Mo^{4+}, whereas those at 230.8 and 233.9 eV was attributed to MoO_x [33]. Figure 3(c) presents the deconvoluted Co $2p_{1/2}$ spectrum of $(NiMo)_{1-x}Co_xO_4$/NF, featuring of a Co^{2+} peak (797.1 eV) and a satellite peak (802.8 eV), while the corresponding Co $2p_{3/2}$ spectrum also featured a Co^{2+} peak (781.3 eV), and a satellite peak (786.3 eV). Upon going from $(NiMo)_{1-x}Co_xO_4$/NF to $(NiMo)_{1-x}Co_xP$/NF (Fig. 3(d)), the Co $2p_{1/2}$ peak (795.5 eV), the Co $2p_{3/2}$ peak (780.3 eV), and two satellite peaks were shifted, revealing the co-existence of Co^{2+} and Co^{3+} after phosphorization [38, 39]. In the P 2p XPS spectrum of $(NiMo)_{1-x}Co_xP$/NF (Fig. S5(c) in the ESM), the P peak located at 129.7 eV was ascribed to metal-bonded P, indicating successful phosphorization and the formation of Ni_2P. The peaks at 133.0 and 134.2 eV were assigned to the P $2p_{3/2}$ and $2p_{1/2}$ transitions of oxidized metal phosphates produced by the superficial oxidation of $(NiMo)_{1-x}Co_xP$ [40–42]. The O peak could be ascribed not only to surface oxidization in ambient air to afford P–O bonds [43], but also to the presence of incompletely phosphatized nanorods in the form of molybdate,

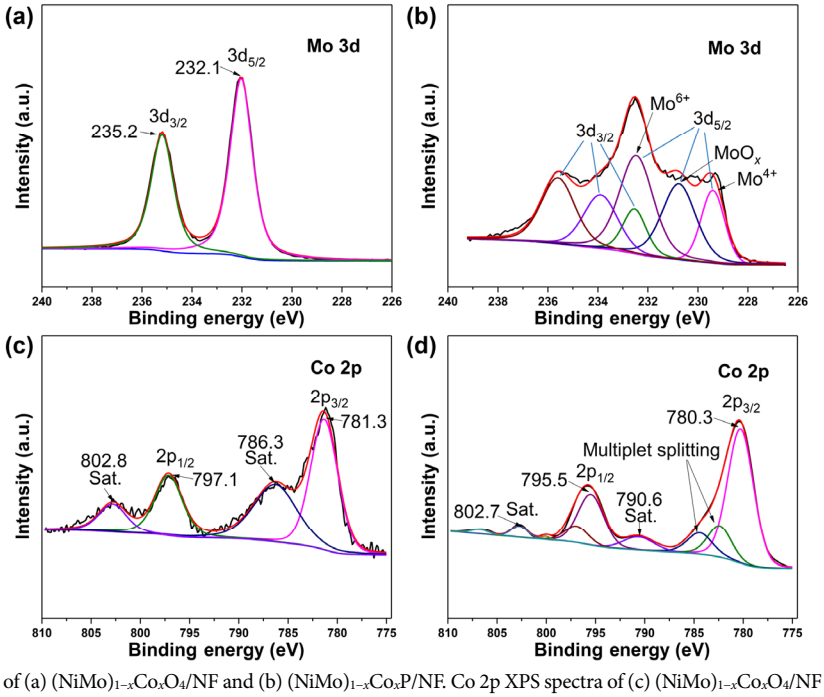

Figure 3 Mo 3d XPS spectra of (a) $(NiMo)_{1-x}Co_xO_4$/NF and (b) $(NiMo)_{1-x}Co_xP$/NF. Co 2p XPS spectra of (c) $(NiMo)_{1-x}Co_xO_4$/NF and (d) $(NiMo)_{1-x}Co_xP$/NF.

as verified by time-of-flight secondary-ion mass spectrometry (TOF-SIMS) mapping (Fig. S5(d) in the ESM), in agreement with the XRD results.

2.2 Electrocatalytic water splitting

Chemical composition and morphology characterization confirmed the successful synthesis of $(NiMo)_{1-x}Co_xP$/NF. To verify the effectiveness of Co doping and phosphorization for electrocatalytic activity enhancement, the catalytic HER performance was assessed by analyzing the *iR*-corrected HER polarization curves (Fig. 4(a)). $(NiMo)_{1-x}Co_xP$/NF required an overpotential of only 29 mV to drive a hydrogen evolution current density of 10 mA·cm^{-2} in Ar-saturated 1.0 M KOH, which was close to the value observed for the state-of-the-art Pt/C on Ni foam catalyst (25 mV) and much lower than the values obtained for other catalysts such as NiMoP/NF (92 mV), $(NiMo)_{1-x}Co_xO_4$/NF (185 mV), $NiMoO_4$/NF (198 mV), CoP/NF (127 mV), and CoC/NF (236 mV). This behavior demonstrated the superiority of $(NiMo)_{1-x}Co_xP$/NF and revealed the effects of phosphorization and Co doping on HER activity. In particular, the overpotential of NiMoP/NF was much lower than that of $(NiMo)_{1-x}Co_xO_4$/NF, indicating that phosphorization played a more important role than Co doping. Moreover, the SEM images of NiMoP/NF and $(NiMo)_{1-x}Co_xO_4$/NF were shown in Fig. S8 in the ESM, where nanorods without rugged and granulated morphologies. Table S1 in the ESM provided a performance comparison for various self-supported HER electrocatalysts recently reported in literature.

The electrocatalytic HER kinetics was quantified in terms of the slope of the Tafel plot for each catalyst (Fig. S9 in the ESM). The slope of $(NiMo)_{1-x}Co_xP$/NF was lower than those of the comparative samples, which is indicative of faster HER kinetics. Electrochemical impedance spectroscopy (EIS) tests were conducted to further confirm the superior electrocatalytic kinetics of $(NiMo)_{1-x}Co_xP$/NF. Usually, a small charge transfer resistance (R_{ct}) signifies fast charge transfer kinetics [44]. The Nyquist plots recorded at an overpotential of 100 mV (Fig. 4(b)) were fitted by an equivalent circuit, and the R_{ct} of $(NiMo)_{1-x}Co_xP$/NF (2.9 Ω) was found to be smaller than those of the comparative samples, such as NiMoP/NF (3.4 Ω). In combination with the catalyst morphologies (Fig. 2(b) and Fig. S8(a) in the ESM), this behavior indicated that the granulated hierarchy of the nanorods favored electron transfer. To estimate the electrochemical surface area, the number of active sites was evaluated using the double-layer capacitance (C_{dl}) obtained by cyclic voltammetry curves (Fig. S10 in the ESM). As shown in Fig. S11 in the ESM, the C_{dl} of $(NiMo)_{1-x}Co_xP$/NF (186.9 mF·cm^{-2}) was slightly higher than that of NiMoP/NF (172 mF·cm^{-2}) and significantly exceeded those of $NiMoO_4$/NF (0.74 mF·cm^{-2}), CoP/NF (4.53 mF·cm^{-2}), and CoC/NF (0.53 mF·cm^{-2}). Thus, the high electrochemical surface area of $(NiMo)_{1-x}Co_xP$/NF resulting from the scaffold-nanorod-granulated surface hierarchy could also contribute to the favorable HER activity. To further clarify the inherent HER activity of $(NiMo)_{1-x}Co_xP$/NF and NiMoP/NF, their linear sweep voltammograms were normalized by the electrochemical active surface area (ECSA). As shown in Fig. S12 in the ESM, the intrinsic activity of $(NiMo)_{1-x}Co_xP$/NF was superior to that of NiMoP/NF. In addition to catalytic activity, long-term durability is also critical for the practical application of self-supported catalysts. Herein, the durability was assessed by recording a chronoamperometric curve at −0.11 V vs. RHE for $(NiMo)_{1-x}Co_xP$/NF (Fig. 4(c)). A sufficient high current density was maintained after 40 h of testing, demonstrating that the HER activity of $(NiMo)_{1-x}Co_xP$/NF was stable in alkaline media. $(NiMo)_{1-x}Co_xP$/NF retained rough and highly interconnected nanorods after long-time HER stability test in Fig. S13 in the ESM.

To understand the origin of the significant Co doping-induced enhancement of the HER activity observed for $(NiMo)_{1-x}Co_xP$/NF, density functional theory was used to calculate the HER Gibbs free energies for $(NiMo)_{1-x}Co_xP$/NF and NiMoP/NF. The optimized structures of H* adsorbed on different sites in the two catalysts are demonstrated in Figs. S14–S16 in the ESM. And the model was built with the 100 surface in the presence of a vacuum layer of 15 A in the *c* direction. In alkaline media,

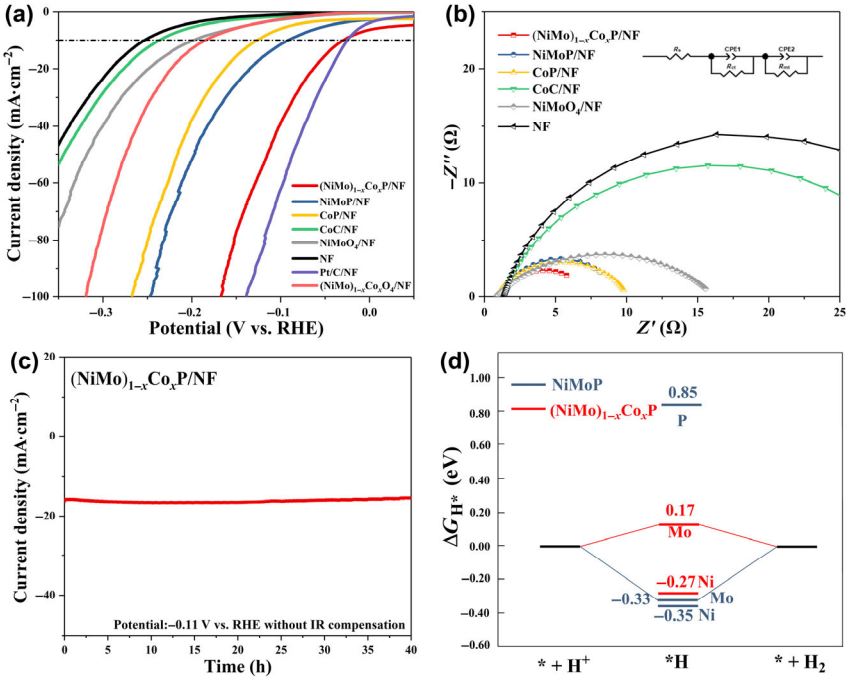

Figure 4 (a) Polarization curves of as-prepared electrodes for the HER in 1.0 M KOH. (b) Nyquist plots of as-prepared electrodes for the HER at η = 100 mV; Inset: corresponding equivalent circuit. (c) Chronoamperometric curve of self-supported $(NiMo)_{1-x}Co_xP$/NF for the HER over 40 h. (d) HER Gibbs free energies for $(NiMo)_{1-x}Co_xP$/NF and NiMoP/NF.

the HER proceeds via three stages: initial catalyst–water adsorbate, intermediate adsorbed hydrogen, and final catalyst–H_2 [45]. The HER activity of a catalyst can be assessed in terms of the Gibbs free energy (ΔG_{H^*}) of the intermediate with adsorbed hydrogen [46]. The optimal performance occurs at $\Delta G_{H^*} \approx 0$ eV, i.e., when the adsorption and dissociation of hydrogen on the catalyst surface are in equilibrium [47]. Figure 4(d) revealed that for NiMoP/NF, the ΔG_{H^*} value at a Mo site (0.33 eV) was lower than those at other sites, indicating that the Mo site was the active site. Further, $(NiMo)_{1-x}Co_xP$/NF featured lower ΔG_{H^*} values than NiMoP/NF, indicating that the former composite had more favorable hydrogen adsorption–desorption behavior. Moreover, for $(NiMo)_{1-x}Co_xP$/NF, the lowest ΔG_{H^*} value was also for a Mo site (0.17 eV), implying that the Mo site remained the active site while Co doping increased the electrocatalytic activity of the NiMoP nanorods. $(NiMo)_{1-x}Co_xP$/NF still retained basic nanorods morphology after long-time OER stability test in Fig. S17 in the ESM.

Since the OER was the other key half-reaction for electrocatalytic water splitting, the OER performances of the as-synthesized samples were also evaluated. As illustrated in Fig. 5(a), a current density of 50 mA·cm^{-2} was achieved at an overpotential of 314 mV for $(NiMo)_{1-x}Co_xP$/NF in oxygen-saturated 1 M KOH. Therefore, this catalyst outperformed RuO_2/NF (393 mV), $(NiMo)_{1-x}Co_xO_4$/NF (389 mV), NiMoP/NF (357 mV), $NiMoO_4$/NF (479 mV), CoP/NF (418 mV), and CoC/NF (471 mV). The overpotential of NiMoP/NF was also lower than that of $(NiMo)_{1-x}Co_xO_4$/NF, which demonstrated that phosphorization had a greater effect on the OER activity than Co doping, similar to the trend observed for the HER. The superior OER performance of $(NiMo)_{1-x}Co_xP$/NF was confirmed by comparing its performance with those of previously reported state-of-the-art OER catalysts (Table S2 in the ESM). An EIS analysis of $(NiMo)_{1-x}Co_xP$/NF performed under OER conditions at an overpotential of 300 mV (Fig. 5(b)) revealed that the R_{ct} of this composite (0.74 Ω) was smaller than those comparative catalysts, including CoP/NF (0.92 Ω), NiMoP/NF (1.67 Ω), and CoC/NF (2.86 Ω), indicating improved charge transportation for the OER. The OER performance stability was evaluated at 1.60 V vs. RHE (Fig. 5(c)), and the corresponding chronoamperometric curve showed no obvious attenuation over 40 h.

However, as transition-metal phosphides are inevitably oxidized under the strong oxidizing conditions of the OER (at least on the surfaces), they should be regard as "precatalysts" [48, 49]. Therefore, to gain further insights into the real active structure for the OER, $(NiMo)_{1-x}Co_xP$/NF was characterized by XRD, XPS, SEM, and HR-TEM after long-term OER tests. In the XRD pattern of $(NiMo)_{1-x}Co_xP$/NF after the OER test (Fig. 5(d)), besides the diffraction peaks of the ineluctable basal Ni foam (JCPDS No. 04-0850), the other diffraction peaks could be indexed to Ni_2P (JCPDS No. 74-1385) and NiO (JCPDS No. 44-1159). As shown in the XPS survey spectrum of $(NiMo)_{1-x}Co_xP$/NF after the OER test (Fig. S18(a) in the

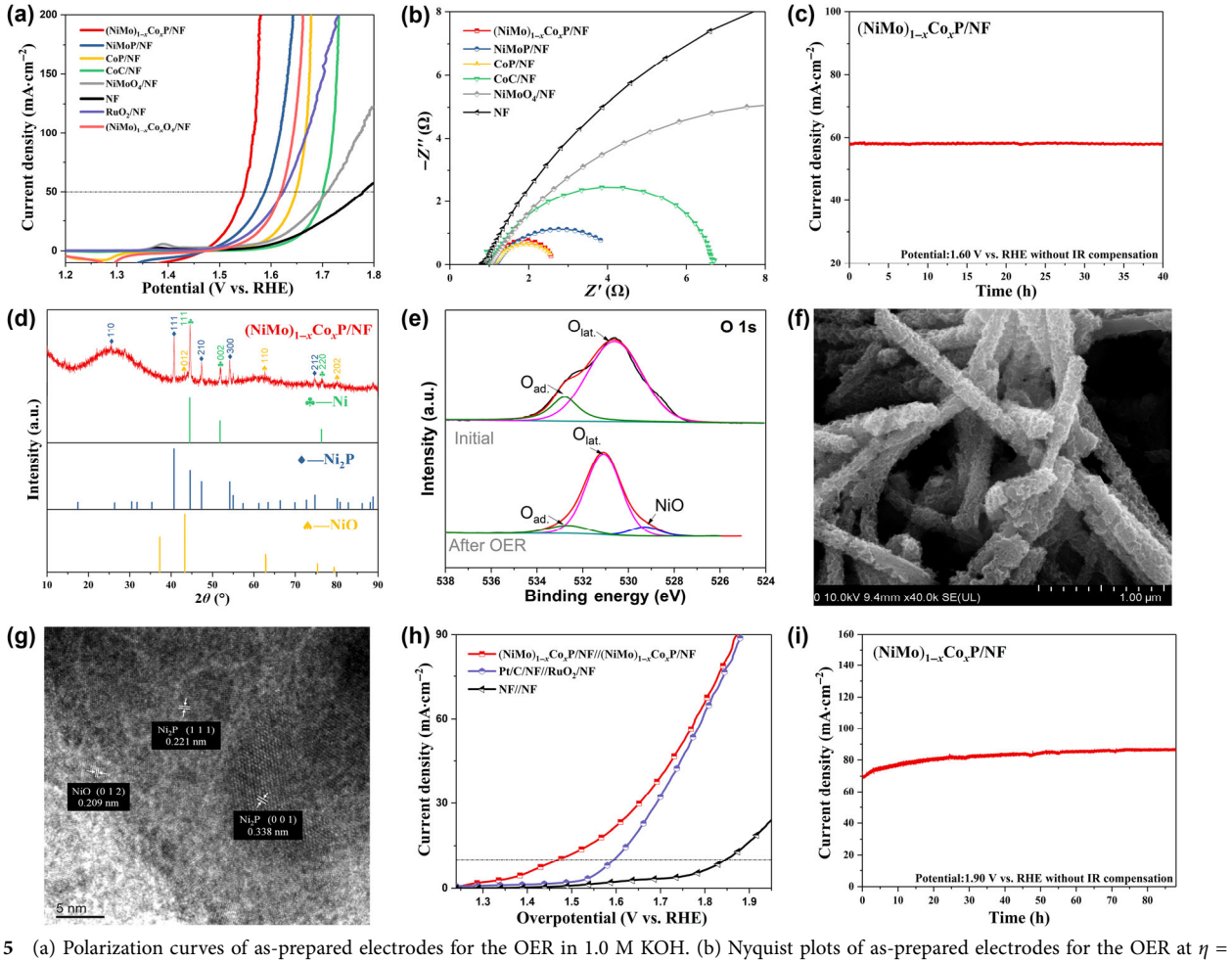

Figure 5 (a) Polarization curves of as-prepared electrodes for the OER in 1.0 M KOH. (b) Nyquist plots of as-prepared electrodes for the OER at η = 300 mV. (c) Chronoamperometric curve of $(NiMo)_{1-x}Co_xP$/NF the OER over 40 h. (d) XRD patterns of $(NiMo)_{1-x}Co_xP$/NF after the OER, Ni, Ni_2P, and NiO. (e) O 1s XPS spectra of $(NiMo)_{1-x}Co_xP$/NF before and after the OER. (f) SEM and (g) HR-TEM images of $(NiMo)_{1-x}Co_xP$/NF after the OER. (h) Polarization curves of $(NiMo)_{1-x}Co_xP$/NF//$(NiMo)_{1-x}Co_xP$/NF, Pt/C/NF//RuO_2/NF, and NF//NF for overall water splitting in 1.0 M KOH. (i) Current density vs. time curve of $(NiMo)_{1-x}Co_xP$/NF//$(NiMo)_{1-x}Co_xP$/NF recorded at a cell voltage of 1.90 V in 1.0 M KOH.

ESM), the O 1s intensity was greatly increased. The high-resolution O 1s XPS spectrum (Fig. 5(e)) further verified the generation of NiO species after the OER, which could be attributed to the *in-situ* electrochemical oxidation of the electrocatalyst [50]. The surface oxidation of the initial phosphide was further confirmed by the attenuation of phosphide signals in the corresponding P 2p XPS spectrum (Fig. S18(b) in the ESM) and the reconversion of all Mo species to Mo^{6+} in the corresponding Mo 3d XPS spectrum (Fig. S18(c) in the ESM) [38, 40]. The SEM image (Fig. 5(f)) and TEM image (Fig. S18(f) in the ESM) suggested that $(NiMo)_{1-x}Co_xP$/NF lost its pristine granulated surface after the OER but retained rough and highly interconnected nanorods. In the corresponding HR-TEM image (Fig. 5(g)), the fringe spacing of 0.209 nm was consistent with the (012) facet of NiO, indicating the formation of a NiO phase on the surface of $(NiMo)_{1-x}Co_xP$/NF. Notably, in recent years, NiO species have been recognized as electrocatalytic active sites for the OER and thus, could contribute to the excellent OER performance of $(NiMo)_{1-x}Co_xP$/NF [51, 52].

The excellent OER and HER performances of $(NiMo)_{1-x}Co_xP$/NF demonstrated its practical applicability as a noble-metal-free electrocatalyst for overall water splitting. Hence, a two-electrode electrolyzer with two $(NiMo)_{1-x}Co_xP$/NF electrodes was assembled and tested under alkaline conditions with *iR* correction. For comparison, an electrolyzer with a Pt/C/NF cathode and RuO_2/NF anode was also tested. As shown in Fig. 5(h), the cell voltage was only 1.47 V at 10 mA·cm^{-2} for $(NiMo)_{1-x}Co_xP$/NF//$(NiMo)_{1-x}Co_xP$/NF, whereas the potential was 1.59 V for Pt/C/NF//RuO_2/NF, indicating the exceptional overall water splitting performance of the former cell. As envisioned, the voltage of the $(NiMo)_{1-x}Co_xP$/NF//$(NiMo)_{1-x}Co_xP$/NF electrolyzer at 10 mA·cm^{-2} was also lower than those of recently reported noble-metal-free catalysts such as $NiCo_2S_4$ NW/NF (1.63 V), $Co_5Mo_{1.0}P$/NF (1.68 V) and NiMoN-450/NF (1.50 V) (Table S3 in the ESM). More importantly, $(NiMo)_{1-x}Co_xP$/NF//$(NiMo)_{1-x}Co_xP$/NF exhibited superior long-term stability even when electrolysis was conducted at 1.90 V (Fig. 5(i)). In this case, the initial current density of 74 mA·cm^{-2} was stabilized at > 86 mA·cm^{-2} during continuous water splitting for 88 h. Thus, the demonstrated long-term stability of $(NiMo)_{1-x}Co_xP$/NF//$(NiMo)_{1-x}Co_xP$/NF at a high current density confirms to the suitability of these noble-metal-free electrocatalysts for overall water splitting applications.

3 Conclusions

Co-doped Ni–Mo phosphide nanorod arrays on Ni foam ($(NiMo)_{1-x}Co_xP$/NF) were synthesized and used as a high-performance self-supported noble-metal-free electrocatalyst. Benefiting from its scaffold-nanorod-granulated surface hierarchical structure and Co doping, the corresponding electrode exhibited high catalytic activity and long-term stability for both HER and OER in alkaline media. The catalyst required an overpotential of 29 mV at 10 mA·cm^{-2} for the HER, whereas the precatalyst required an overpotential of and 314 mV at 50 mA·cm^{-2} for the OER. A two-electrode water splitting electrolyzer assembled with $(NiMo)_{1-x}Co_xP$/NF electrodes exhibited a cell voltage of 1.47 V at 10 mA·cm^{-2}. Notably, this water-splitting performance is superior to that of the benchmark Pt/C and RuO_2 couple. Furthermore, long-term stability testing at a high current density revealed no performance decay within 88 h. Thus, $(NiMo)_{1-x}Co_xP$/NF, prepared by Co-doping and surface phosphorization, shows considerable promising as a water-splitting electrocatalyst.

4 Experimental

4.1 Materials

$NiCl_2·6H_2O$, $Co(NO_3)_2·6H_2O$, $Na_2MoO_4·2H_2O$, and KOH were purchased from Shanghai Aladdin Biological Technology Co., Ltd. Ni foam, Pt/C (20 wt.%), RuO_2, red phosphorus, 2-methylimidazole, and Nafion (5 wt.%) were obtained from Sinopharm Chemical Reagent Co., Ltd. All the chemicals were of analytical grade and were used without further purification. All the aqueous solutions were prepared using ultrapure water (> 18.2 MΩ·cm).

4.2 Synthesis of $NiMoO_4$/NF

Ni foam (1 cm × 1.5 cm, 380 g·m^{-2}) was degreased via sonication in acetone and ethanol and then annealed at 500 °C in H_2/Ar (1:9, v/v; 1.5 Torr) to fully remove the surface native oxide layer. $NiMoO_4$ nanowire arrays on the Ni foam substrate ($NiMoO_4$/NF) were synthesized via the following hydrothermal process [53]. $NiCl_2·6H_2O$ and $Na_2MoO_4·2H_2O$ (1 mmol each) were dissolved in water (15 mL) under vigorous stirring for 60 min. The solution was transferred to a Teflon-lined stainless autoclave with the annealed Ni foam, heated at 160 °C for 6 h, and naturally cooled to room temperature. The green solid was washed three times with distilled water and ethanol and then dried in a vacuum oven at 60 °C over night.

4.3 Synthesis of $(NiMo)_{1-x}Co_xO_4$/NF

Typically, 2-methylimidazole (4 mmol) was dispersed in methanol (25 mL), and the dispersion was mixed with methanolic $Co(NO_3)_2·6H_2O$ (1 mmol in 25 mL methanol) by stirring [20]. Subsequently, $NiMoO_4$/NF was immersed in this solution and allowed to react for 24 h. When the reaction was finished, the sample was removed and washed with methanol several times to obtain $(NiMo)_{1-x}Co_xO_4$/NF.

4.4 Synthesis of $(NiMo)_{1-x}Co_xP$/NF

Red phosphorus (20 mg) was placed at an upstream side of the tube furnace, and the $(NiMo)_{1-x}Co_xO_4$/NF precursor was placed at the downstream side. The samples were heated to 500 °C at a rate of 2 °C·min^{-1}, maintained for 90 min in a flow of Ar (1.5 Torr), and then cooled to ambient temperature to afford $(NiMo)_{1-x}Co_xP$/NF. Concomitantly, the Ni foam turned black.

4.5 Syntheses of NF-supported catalysts for comparison

$NiMoO_4$/NF, NiMoP/NF, $(NiMo)_{1-x}Co_xO_4$/NF, CoC/NF, and CoP/NF were prepared using the same procedures as employed for the synthesis of $NiMoO_4$/NF and $(NiMo)_{1-x}Co_xO_4$/NF. As-prepared NiMoP/NF and CoP/NF were annealed in the presence of red phosphorus, as described for $(NiMo)_{1-x}Co_xP$/NF, whereas the annealing of $NiMoO_4$/NF, $(NiMo)_{1-x}Co_xO_4$/NF and CoC/NF was performed similarly without red phosphorus.

Pt/C/NF (20 wt.%) and RuO_2/NF catalysts (10 mg) were prepared by 30-min ultrasonication-assisted dispersion of the corresponding solids in a mixture of Nafion solution (5 wt.%; 50 μL), ethanol (450 μL), and distilled water (500 μL) to form homogeneous catalyst ink. Next, 300 μL of each ink was carefully dropped onto annealed Ni foam (1 cm × 1.5 cm), which was then air-dried at ambient temperature.

4.6 Characterization

XRD patterns were recorded on a Bruker D8 Advance instrument using Cu Kα radiation (λ = 1.5418 Å). SEM images were acquired on a FEI Inspect F50 instrument. TEM images,

HAADF-STEM images, and EDX elemental mappings were acquired on a FEI Talos F200x transmission electron microscope equipped with an energy-dispersive X-ray detector. XPS was conducted using a Thermo Fischer Escalab 250Xi spectrophotometer with monochromatic Al Kα radiation. TOF-SIMS mapping was performed using an IONTOF GmbH 5 instrument with a pulsed bismuth liquid metal ion gun at an incident angle of 50° to reveal the 2D molecular distribution of $(NiMo)_{1-x}Co_xP$/NF (100 μm × 100 μm).

4.7 Electrochemical measurements

Electrochemical measurements were performed using a Solartron 1260+1287 electrochemical analyzer (Solartron Metrology, UK) in Ar- (HER) or O_2- (OER) saturated 1.0 M aqueous KOH at ambient temperature. A standard three-electrode system was used with a graphite rod and Ag/AgCl (sat. KCl) as counter and reference electrodes, respectively. The synthesized samples were directly used as the working electrode without any binder or conductive agent, and the electrode area was controlled at 1 cm^2. To active the electrode, hundreds of potential cycles were carried out until the signal was stabilized. Linear sweep voltammetry was performed over the voltage range from 1.0 to 1.8 V (vs. RHE) for the OER and from −0.6 to 0.1 V (vs. RHE) for the HER at a slow scan rate of 2 $mV \cdot s^{-1}$ to minimize the capacitive current. All the potentials vs. Ag/AgCl were referenced to the RHE scale using the Nernst equation: $E_{RHE} = E_{Ag/AgCl} + 0.0591pH + 0.197$. Subsequently, the potentials were corrected according to the ohmic potential drop (iR) based on the series resistances derived from the electrochemical impedance spectra. EIS was conducted at an overpotential of 100 mV for the HER and 300 mV for the OER in the frequency range 0.01–100 kHz. The equivalent circuit for EIS data fitting was derived using ZView software. Polarization curves were replotted as overpotential (η) vs. logarithm of absolute current density (log $|j|$) to obtain Tafel plots. η was calculated as $E_{RHE} - E_r$, where E_r equals 1.23 V (vs. RHE) for the OER and 0 V (vs. RHE) for the HER. The electrochemical surface area of each electrode was related to the double-layer charging curve using cyclic voltammetry in the potential ranges 0.2–0.3 V and 1.0–1.1 V (vs. RHE) for the HER and OER, respectively. The C_{dl} was determined from the slope of the capacitive current vs. scan rate plot. For the intrinsic activity of catalysts, linear sweep voltammograms were normalized by the corresponding ECSA values, which were estimated from the C_{dl} values using the following equation: ECSA = C_{dl}/C_s, where C_s is the specific capacitance of the sample or the capacitance of an atomically smooth planar surface of the material per unit area under identical electrolyte conditions [54–56]. As C_s is normally between 20 and 60 $\mu F \cdot cm^{-2}$, an average value of 40 $\mu F \cdot cm^{-2}$ was used in the calculation. Overall water splitting was performed in a two-electrode electrochemical system without iR compensation.

4.8 Density functional theory calculations

Vienna *ab initio* simulation package (VASP) software [57, 58] and the Perdew–Burke–Ernzerhof (PBE) functional [59] were employed for calculations. The ENCUT parameter was set at 400 eV. A 11.7 Å × 7.4 Å × 29.0 Å slab model was built to model the (100) surface of NiMoP/NF, with a vacuum layer of 15 Å in the z-direction. The reciprocal space was integrated with a 1 × 2 × 1 k-mesh generated under the gamma scheme.

Acknowledgements

This work was supported by the National Natural Science Foundation of China (No. 51827901). We would like to thank the Institute of New Energy and Low-Carbon Technology, Sichuan University, for XRD analysis work. We also thank Clean Energy Research Institute for the support.

Electronic Supplementary Material: Supplementary material (additional catalyst characterization) is available in the online version of this article at https://doi.org/10.1007/s12274-020-3010-7.

References

[1] Ming, M.; Zhang, Y.; He, C.; Zhao, L.; Niu, S.; Fang, G. Y.; Hu, J. S. Room-temperature sustainable synthesis of selected platinum group metal (PGM = Ir, Rh, and Ru) nanocatalysts well-dispersed on porous carbon for efficient hydrogen evolution and oxidation. *Small* **2019**, *15*, 1903057.

[2] Cheng, H.; Su, Y. Z.; Kuang, P. Y.; Chen, G. F.; Liu, Z. Q. Hierarchical $NiCo_2O_4$ nanosheet-decorated carbon nanotubes towards highly efficient electrocatalyst for water oxidation. *J. Mater. Chem. A* **2015**, *3*, 19314–19321.

[3] Lu, W. B.; Liu, T. T.; Xie, L. S.; Tang, C.; Liu, D. N.; Hao, S.; Qu, F. L.; Du, G.; Ma, Y. J.; Asiri, A. M.; et al. *In situ* derived Co–B nanoarray: A high-efficiency and durable 3D bifunctional electrocatalyst for overall alkaline water splitting. *Small* **2017**, *13*, 1700805.

[4] Faber, M. S.; Jin, S. Earth-abundant inorganic electrocatalysts and their nanostructures for energy conversion applications. *Energy Environ. Sci.* **2014**, *7*, 3519–3542.

[5] Subbaraman, R.; Tripkovic, D.; Strmcnik, D.; Chang, K. C.; Uchimura, M.; Paulikas, A. P.; Stamenkovic, V.; Markovic, N. M. Enhancing hydrogen evolution activity in water splitting by tailoring Li^+-$Ni(OH)_2$-Pt interfaces. *Science* **2011**, *334*, 1256–1260.

[6] Yang, L.; Guo, Z. L.; Huang, J.; Xi, Y. N.; Gao, R. J.; Su, G.; Wang, W.; Cao, L. X.; Dong, B. H. Vertical growth of 2D amorphous $FePO_4$ nanosheet on Ni foam: Outer and inner structural design for superior water splitting. *Adv. Mater.* **2017**, *29*, 1704574.

[7] Han, L.; Dong, S. J.; Wang, E. K. Transition-metal (Co, Ni, and Fe)-based electrocatalysts for the water oxidation reaction. *Adv. Mater.* **2016**, *28*, 9266–9291.

[8] Anantharaj, S.; Ede, S. R.; Sakthikumar, K.; Karthick, K.; Mishra, S.; Kundu, S. Recent trends and perspectives in electrochemical water splitting with an emphasis on sulfide, selenide, and phosphide catalysts of Fe, Co, and Ni: A review. *ACS Catal.* **2016**, *6*, 8069–8097.

[9] Yan, Y.; Xia, B. Y.; Zhao, B.; Wang, X. A review on noble-metal-free bifunctional heterogeneous catalysts for overall electrochemical water splitting. *J. Mater. Chem. A* **2016**, *4*, 17587–17603.

[10] Sun, H. M.; Yan, Z. H.; Liu, F. M.; Xu, W. C.; Cheng, F. Y.; Chen, J. Self-supported transition-metal-based electrocatalysts for hydrogen and oxygen evolution. *Adv. Mater.* **2020**, *32*, 1806326.

[11] Faber, M. S.; Dziedzic, R.; Lukowski, M. A.; Kaiser, N. S.; Ding, Q.; Jin, S. High-performance electrocatalysis using metallic cobalt pyrite (CoS_2) micro-and nanostructures. *J. Am. Chem. Soc.* **2014**, *136*, 10053–10061.

[12] Feng, L. L.; Yu, G. T.; Wu, Y. Y.; Li, G. D.; Li, H.; Sun, Y. H.; Asefa, T.; Chen, W.; Zou, X. X. High-index faceted Ni_3S_2 nanosheet arrays as highly active and ultrastable electrocatalysts for water splitting. *J. Am. Chem. Soc.* **2015**, *137*, 14023–14026.

[13] Yu, J. Y.; Li, G. X.; Liu, H.; Zhao, L. L.; Wang, A. Z.; Liu, Z.; Li, H. D.; Liu, H.; Hu, Y. Y.; Zhou, W. J. Ru–Ru_2PΦNPC and NPC@RuO_2 synthesized via environment-friendly and solid-phase phosphating process by saccharomycetes as N/P sources and carbon template for overall water splitting in acid electrolyte. *Adv. Funct. Mater.* **2019**, *29*, 1901154.

[14] Chen, Y. K.; Yu, J. Y.; Jia, J.; Liu, F.; Zhang, Y. W.; Xiong, G. W.; Zhang, R. T.; Yang, R. Q.; Sun, D. H.; Liu, H. et al. Metallic Ni_3Mo_3N porous microrods with abundant catalytic sites as efficient electrocatalyst for large current density and superstability of hydrogen evolution reaction and water splitting. *Appl. Catal. B: Environ.* **2020**, *272*, 118956.

[15] Shan, J. Q.; Ling, T.; Davey, K.; Zheng, Y.; Qiao, S. Z. Transition-metal-doped RuIr bifunctional nanocrystals for overall water splitting in acidic environments. *Adv. Mater.* **2019**, *31*, 1900510.

[16] Xie, L. S.; Qu, F. L.; Liu, Z. A.; Ren, X.; Hao, S.; Ge, R. X.; Du, G.; Asiri, A. M.; Sun, X. P.; Chen, L. *In situ* formation of a 3D core/shell structured Ni_3N@Ni–Bi nanosheet array: An efficient non-noble-metal bifunctional electrocatalyst toward full water splitting under near-neutral conditions. *J. Mater. Chem. A* **2017**, *5*, 7806–7810.

[17] Xiong, Q. Z.; Zhang, X.; Wang, H. J.; Liu, G. Q.; Wang, G. Z.; Zhang, H. M.; Zhao, H. J. One-step synthesis of cobalt-doped MoS_2 nanosheets as bifunctional electrocatalysts for overall water splitting under both acidic and alkaline conditions. *Chem. Commun.* **2018**, *54*, 3859–3862.

[18] Wu, Z. C.; Zou, Z. X.; Huang, J. S.; Gao, F. Fe-doped NiO mesoporous nanosheets array for highly efficient overall water splitting. *J. Catal.* **2018**, *358*, 243–252.

[19] Yuan, C. Z.; Zhong, S. L.; Jiang, Y. F.; Yang, Z. K.; Zhao, Z. W.; Zhao, S. J.; Jiang, N.; Xu, A. W. Direct growth of cobalt-rich cobalt phosphide catalysts on cobalt foil: An efficient and self-supported bifunctional electrode for overall water splitting in alkaline media. *J. Mater. Chem. A* **2017**, *5*, 10561–10566.

[20] Shan, X. Y.; Liu, J.; Mu, H. R.; Xiao, Y.; Mei, B. B.; Liu, W. G.; Lin, G.; Jiang, Z.; Wen, L. P.; Jiang, L. An engineered superhydrophilic/superaerophobic electrocatalyst composed of the supported $CoMoS_x$ chalcogel for overall water splitting. *Angew. Chem., Int. Ed.* **2020**, *59*, 1659–1665.

[21] Zhu, X. Y.; Zhang, X. P.; Huang, L.; Liu, Y. Q.; Zhang, H.; Dong, S. J. Cobalt doped β-molybdenum carbide nanoparticles encapsulated within nitrogen-doped carbon for oxygen evolution. *Chem. Commun.* **2019**, *55*, 9995–9998.

[22] Li, G. X.; Wang, J. G.; Yu, J. Y.; Liu, H.; Cao, Q.; Du, J. L.; Zhao, L. L.; Jia, J.; Liu, H.; Zhou, W. J. Ni-Ni_3P nanoparticles embedded into N, P-doped carbon on 3D graphene frameworks via *in situ* phosphatization of saccharomycetes with multifunctional electrodes for electrocatalytic hydrogen production and anodic degradation. *Appl. Catal. B: Environ.* **2020**, *261*, 118147.

[23] Yu, X. B.; Zhang, S.; Li, C. Y.; Zhu, C. L.; Chen, Y. J.; Gao, P.; Qi, L. H.; Zhang, X. T. Hollow CoP nanopaticle/N-doped graphene hybrids as highly active and stable bifunctional catalysts for full water splitting. *Nanoscale* **2016**, *8*, 10902–10907.

[24] Yin, Z. X.; Zhu, C. L.; Li, C. Y.; Zhang, S.; Zhang, X. T.; Chen, Y. J. Hierarchical nickel–cobalt phosphide yolk–shell spheres as highly active and stable bifunctional electrocatalysts for overall water splitting. *Nanoscale* **2016**, *8*, 19129–19138.

[25] Liu, T. T.; Xie, L. S.; Yang, J. H.; Kong, R. M.; Du, G.; Asiri, A. M.; Sun, X. P.; Chen, L. Self-standing CoP nanosheets array: A three-dimensional bifunctional catalyst electrode for overall water splitting in both neutral and alkaline media. *ChemElectroChem* **2017**, *4*, 1840–1845.

[26] Hu, E. L.; Feng, Y. F.; Nai, J. W.; Zhao, D. A.; Hu, Y.; Lou, X. W. Construction of hierarchical Ni–Co–P hollow nanobricks with oriented nanosheets for efficient overall water splitting. *Energy Environ. Sci.* **2018**, *11*, 872–880.

[27] Liu, T. T.; Liu, D. N.; Qu, F. L.; Wang, D. X.; Zhang, L.; Ge, R. X.; Hao, S.; Ma, Y. J.; Du, G.; Asiri, A. M. et al. Enhanced electrocatalysis for energy-efficient hydrogen production over CoP catalyst with nonelectroactive Zn as a promoter. *Adv. Energy Mater.* **2017**, *7*, 1700020.

[28] Liu, P.; Rodriguez, J. A. Catalysts for hydrogen evolution from the [NiFe] hydrogenase to the Ni_2P(001) surface: The importance of ensemble effect. *J. Am. Chem. Soc.* **2005**, *127*, 14871–14878.

[29] Ledendecker, M.; Calderón, S. K.; Papp, C.; Steinrück, H. P.; Antonietti, M.; Shalom, M. The synthesis of nanostructured Ni_5P_4 films and their use as a non-noble bifunctional electrocatalyst for full water splitting. *Angew. Chem., Int. Ed.* **2015**, *54*, 12361–12365.

[30] Li, K.; Rakov, D.; Zhang, W.; Xu, P. Improving the intrinsic electrocatalytic hydrogen evolution activity of few-layer $NiPS_3$ by cobalt doping. *Chem. Commun.* **2017**, *53*, 8199–8202.

[31] Fu, S. F.; Zhu, C. Z.; Song, J. H.; Engelhard, M. H.; Li, X. L.; Du, D.; Lin, Y. H. Highly ordered mesoporous bimetallic phosphides as efficient oxygen evolution electrocatalysts. *ACS Energy Lett.* **2016**, *1*, 792–796.

[32] Liang, X.; Zheng, B. X.; Chen, L. G.; Zhang, J. T.; Zhuang, Z. B.; Chen, B. H. MOF-derived formation of Ni_2P–CoP bimetallic phosphides with strong interfacial effect toward electrocatalytic water splitting. *ACS Appl. Mater. Interfaces* **2017**, *9*, 23222–23229.

[33] Wang, Y.; Sun, Y.; Yan, F.; Zhu, C. L.; Gao, P.; Zhang, X. T.; Chen, Y. J. Self-supported NiMo-based nanowire arrays as bifunctional electrocatalysts for full water splitting. *J. Mater. Chem. A* **2018**, *6*, 8479–8487.

[34] McKone, J. R.; Sadtler, B. F.; Werlang, C. A.; Lewis, N. S.; Gray, H. B. Ni–Mo nanopowders for efficient electrochemical hydrogen evolution. *ACS Catal.* **2013**, *3*, 166–169.

[35] Wang, Y.; Wang, M. Y.; Zhang, Z. S.; Wang, Q.; Jiang, Z.; Lucero, M.; Zhang, X.; Li, X. X.; Gu, M.; Feng, Z. X. et al. Phthalocyanine precursors to construct atomically dispersed iron electrocatalysts. *ACS Catal.* **2019**, *9*, 6252–6261.

[36] Zhang, Y.; Liu, Y. W.; Ma, M.; Ren, X.; Liu, Z. A.; Du, G.; Asiri, A. M.; Sun, X. P. A Mn-doped Ni_2P nanosheet array: An efficient and durable hydrogen evolution reaction electrocatalyst in alkaline media. *Chem. Commun.* **2017**, *53*, 11048–11051.

[37] Du, Z. H.; Zhao, H. L.; Yi, S.; Xia, Q.; Gong, Y.; Zhang, Y.; Cheng, X.; Li, Y.; Gu, L.; Świerczek, K. High-performance anode material $Sr_2FeMo_{0.65}Ni_{0.35}O_{6-\delta}$ with *in situ* exsolved nanoparticle catalyst. *ACS Nano* **2016**, *10*, 8660–8669.

[38] Wei, X. J.; Zhang, Y. H.; He, H. C.; Gao, D.; Hu, J. R.; Peng, H. R.; Peng, L.; Xiao, S. H.; Xiao, P. Carbon-incorporated NiO/Co_3O_4 concave surface microcubes derived from a MOF precursor for overall water splitting. *Chem. Commun.* **2019**, *55*, 6515–6518.

[39] Moosavifard, S. E.; Fani, S.; Rahmanian, M. Hierarchical $CuCo_2S_4$ hollow nanoneedle arrays as novel binder-free electrodes for high-performance asymmetric supercapacitors. *Chem. Commum.* **2016**, *52*, 4517–4520.

[40] He, L. H.; Zhang, S.; Ji, H. F.; Wang, M. H.; Peng, D. L.; Yan, F. F.; Fang, S. M.; Zhang, H. Z.; Jia, C. X.; Zhang, Z. H. Protein-templated cobaltous phosphate nanocomposites for the highly sensitive and selective detection of platelet-derived growth factor-BB. *Biosens. Bioelectron.* **2016**, *79*, 553–560.

[41] Zhang, R.; Wang, X. X.; Yu, S. J.; Wen, T.; Zhu, X. W.; Yang, F. X.; Sun, X. N.; Wang, X. K.; Hu, W. P. Ternary $NiCo_2P_x$ nanowires as pH-universal electrocatalysts for highly efficient hydrogen evolution reaction. *Adv. Mater.* **2017**, *29*, 1605502.

[42] Gong, Y. Q.; Xu, Z. F.; Pan, H. L.; Lin, Y.; Yang, Z.; Wang, J. L. A 3D well-matched electrode pair of Ni–Co–S//Ni–Co–P nanoarrays grown on nickel foam as a high-performance electrocatalyst for water splitting. *J. Mater. Chem. A* **2018**, *6*, 12506–12514.

[43] Deng, Y. Q.; Yang, L. J.; Wang, Y. K.; Zeng, L. L.; Yu, J. Y.; Chen, B.; Zhang, X. L.; Zhou, W. J. Ruthenium nanoclusters anchored on cobalt phosphide hollow microspheres by green phosphating process for full water splitting in acidic electrolyte. *Chin. Chem. Lett.*, in press, DOI: 10.1016/j.cclet.2020.03.076.

[44] Zhao, Y. Q.; Jin, B.; Vasileff, A.; Jiao, Y.; Qiao, S. Z. Interfacial nickel nitride/sulfide as a bifunctional electrode for highly efficient overall water/seawater electrolysis. *J. Mater. Chem. A* **2019**, *7*, 8117–8121.

[45] Chen, P. Z.; Xu, K.; Tao, S.; Zhou, T. P.; Tong, Y.; Ding, H.; Zhang, L. D.; Chu, W. S.; Wu, C. Z.; Xie, Y. Phase-transformation engineering in cobalt diselenide realizing enhanced catalytic activity for hydrogen evolution in an alkaline medium. *Adv. Mater.* **2016**, *28*, 7527–7532.

[46] Zheng, Y.; Jiao, Y.; Zhu, Y. H.; Li, L. H.; Han, Y.; Chen, Y.; Du, A. J.; Jaroniec, M.; Qiao, S. Z. Hydrogen evolution by a metal-free electrocatalyst. *Nat. Commun.* **2014**, *5*, 3783.

[47] Deng, R.; Chen, Q.; Luo, Q.; Zhou, L. X.; Wang, Y.; Zhang, Y.; Fan, G. Y. Salt template-assisted *in situ* construction of Ru nanoclusters and porous carbon: Excellent catalysts toward hydrogen evolution, ammonia-borane hydrolysis, and 4-nitrophenol reduction. *Green Chem.* **2020**, *22*, 835–842.

[48] Jin, S. Are metal chalcogenides, nitrides, and phosphides oxygen evolution catalysts or bifunctional catalysts? *ACS Energy Lett.* **2017**, *2*, 1937–1938.

[49] Luo, X.; Ji, P. X.; Wang, P. Y.; Cheng, R. L.; Chen, D.; Lin, C.; Zhang, J. N.; He, J. W.; Shi, Z. H.; Li, N. et al. Interface engineering of hierarchical branched Mo-doped Ni_3S_2/Ni_xP_y hollow heterostructure

nanorods for efficient overall water splitting. *Adv. Energy Mater.* **2020**, *10*, 1903891.

[50] Tang, C.; Cheng, N. Y.; Pu, Z. H.; Xing, W.; Sun, X. P. NiSe nanowire film supported on nickel foam: An efficient and stable 3D bifunctional electrode for full water splitting. *Angew. Chem., Int. Ed.* **2015**, *54*, 9351–9355.

[51] Zeng, L. Y.; Sun, K. A.; Wang, X. B.; Liu, Y. Q.; Pan, Y.; Liu, Z.; Cao, D. W.; Song, Y.; Liu, S. H.; Liu, C. G. Three-dimensional-networked Ni_2P/Ni_3S_2 heteronanoflake arrays for highly enhanced electrochemical overall-water-splitting activity. *Nano Energy* **2018**, *51*, 26–36.

[52] Stern, L. A.; Feng, L. G.; Song, F.; Hu, X. L. Ni_2P as a Janus catalyst for water splitting: The oxygen evolution activity of Ni_2P nanoparticles. *Energy Environ. Sci.* **2015**, *8*, 2347−2351.

[53] Sun, Y. Q.; Hang, L. F.; Shen, Q.; Zhang, T.; Li, H. L.; Zhang, X. M.; Lyu, X. J.; Li, Y. Mo doped Ni_2P nanowire arrays: An efficient electrocatalyst for the hydrogen evolution reaction with enhanced activity at all pH values. *Nanoscale* **2017**, *9*, 16674–16679.

[54] Lukowski, M. A.; Daniel, A. S.; English, C. R.; Meng, F.; Forticaux, A.; Hamers, R. J.; Jin, S. Highly active hydrogen evolution catalysis from metallic WS_2 nanosheets. *Energy Environ. Sci.* **2014**, *7*, 2608–2613.

[55] Liang, H. F.; Gandi, A. N.; Anjum, D. H.; Wang, X. B.; Schwingenschlögl, U.; Alshareef, H. N. Plasma-assisted synthesis of NiCoP for efficient overall water splitting. *Nano Lett.* **2016**, *16*, 7718–7725.

[56] Du, C.; Yang, L.; Yang, F. L.; Cheng, G. Z.; Luo, W. Nest-like NiCoP for highly efficient overall water splitting. *ACS Catal.* **2017**, *7*, 4131–4137.

[57] Kresse, G.; Furthmüller, J. Efficient iterative schemes for *ab initio* total-energy calculations using a plane-wave basis set. *Phys. Rev. B* **1996**, *54*, 11169–11186.

[58] Kresse, G.; Furthmüller, J. Efficiency of *ab-initio* total energy calculations for metals and semiconductors using a plane-wave basis set. *Comput. Mater. Sci.* **1996**, *6*, 15–50.

[59] Perdew, J. P.; Burke, K.; Ernzerhof, M. Generalized gradient approximation made simple. *Phys. Rev. Lett.* **1996**, *77*, 3865–3868.